

1 The Silicon Vertex Detector of the Belle II Experiment

2 Y. Uematsu^a, K. Adamczyk^t, L. Aggarwal^l, H. Aihara^q, T. Aziz^j, S. Bacher^t,
3 S. Bahinipati^f, G. Batignani^{k,l}, J. Baudot^e, P. K. Behera^g, S. Bettarini^{k,l},
4 T. Bilka^c, A. Bozek^t, F. Buchsteiner^b, G. Casarosa^{k,l}, L. Corona^{k,l}, T. Czank^p,
5 S. B. Das^h, G. Dujany^e, C. Finck^e, F. Forti^{k,l}, M. Friedl^b, A. Gabrielli^{m,n},
6 E. Ganiev^{m,n}, B. Gobboⁿ, S. Halder^j, K. Hara^{r,o}, S. Hazra^j, T. Higuchi^p,
7 C. Irmeler^b, A. Ishikawa^{r,o}, H. B. Jeon^s, Y. Jin^{m,n}, C. Joo^p, M. Kaleta^t,
8 A. B. Kaliyar^j, J. Kandra^c, K. H. Kang^s, P. Kapusta^t, P. Kodyš^c, T. Kohriki^r,
9 M. Kumar^h, R. Kumarⁱ, C. La Licata^p, K. Lalwani^h, R. Le Boucher^d,
10 S. C. Lee^s, J. Libby^g, L. Martel^e, L. Massacesi^{k,l}, S. N. Mayekar^j,
11 G. B. Mohanty^j, T. Morii^p, K. R. Nakamura^{r,o}, Z. Natkaniec^t, Y. Onuki^q,
12 W. Ostrowicz^t, A. Paladino^{k,l}, E. Paoloni^{k,l}, H. Park^s, G. Polat^d, K. K. Rao^j,
13 I. Ripp-Baudot^e, G. Rizzo^{k,l}, D. Sahoo^j, C. Schwanda^b, J. Serrano^d,
14 J. Suzuki^r, S. Tanaka^{r,o}, H. Tanigawa^q, R. Thalmeier^b, R. Tiwari^j,
15 T. Tsuboyama^{r,o}, O. Verbycka^t, L. Vitale^{m,n}, K. Wan^q, Z. Wang^q, J. Webb^a,
16 J. Wiechczynski^l, H. Yin^b, L. Zani^d,

17 (Belle-II SVD Collaboration)

18 ^a*School of Physics, University of Melbourne, Melbourne, Victoria 3010, Australia*

19 ^b*Institute of High Energy Physics, Austrian Academy of Sciences, 1050 Vienna, Austria*

20 ^c*Faculty of Mathematics and Physics, Charles University, 121 16 Prague, Czech Republic*

21 ^d*Aix Marseille Université, CNRS/IN2P3, CPPM, 13288 Marseille, France*

22 ^e*IPHC, UMR 7178, Université de Strasbourg, CNRS, 67037 Strasbourg, France*

23 ^f*Indian Institute of Technology Bhubaneswar, Satya Nagar, India*

24 ^g*Indian Institute of Technology Madras, Chennai 600036, India*

25 ^h*Malaviya National Institute of Technology Jaipur, Jaipur 302017, India*

26 ⁱ*Punjab Agricultural University, Ludhiana 141004, India*

27 ^j*Tata Institute of Fundamental Research, Mumbai 400005, India*

28 ^k*Dipartimento di Fisica, Università di Pisa, I-56127 Pisa, Italy*

29 ^l*INFN Sezione di Pisa, I-56127 Pisa, Italy*

30 ^m*Dipartimento di Fisica, Università di Trieste, I-34127 Trieste, Italy*

31 ⁿ*INFN Sezione di Trieste, I-34127 Trieste, Italy*

32 ^o*The Graduate University for Advanced Studies (SOKENDAI), Hayama 240-0193, Japan*

33 ^p*Kavli Institute for the Physics and Mathematics of the Universe (WPI), University of*

34 *Tokyo, Kashiwa 277-8583, Japan*

35 ^q*Department of Physics, University of Tokyo, Tokyo 113-0033, Japan*

36 ^r*High Energy Accelerator Research Organization (KEK), Tsukuba 305-0801, Japan*

37 ^s*Department of Physics, Kyungpook National University, Daegu 41566, Korea*

38 ^t*H. Niewodniczanski Institute of Nuclear Physics, Krakow 31-342, Poland*

39 Abstract

40 The Silicon Vertex Detector (SVD) is a part of the vertex detector in the
41 Belle II experiment at the SuperKEKB collider (KEK, Japan). Since the start
42 of data taking in spring 2019, the SVD has been operating stably and reliably

43 with a high signal-to-noise ratio and hit efficiency, achieving good spatial resolu-
44 tion and high track reconstruction efficiency. The hit occupancy, which mostly
45 comes from the beam-related background, is currently about 0.5% in the in-
46 nermost layer, causing no impact on the SVD performance. In anticipation of
47 the operation at higher luminosity in the next years, two strategies to sustain
48 the tracking performance in future high beam background conditions have been
49 developed and tested on data. One is to reduce the number of signal waveform
50 samples to decrease dead time, data size, and occupancy. The other is to utilize
51 the good hit-time resolution to reject the beam background hits. We also mea-
52 sured the radiation effects on the sensor current, strip noise, and full depletion
53 voltage caused during the first two and a half years of operation. The results
54 show no detrimental effect on the SVD performance.

55 *Keywords:* Silicon strip detector, Vertex detector, Tracking detector, Belle II

56 1. Introduction

57 The Belle II experiment [1] aims to probe new physics beyond the Standard
58 Model in high-luminosity e^+e^- collisions at the SuperKEKB collider (KEK,
59 Japan) [2]. SuperKEKB consists of the following components: injector LINAC,
60 positron damping ring, and main storage ring with the electron and positron
61 beamlines. The Belle II detector is located at the interaction point (IP) of
62 the two beamlines. The main collision energy in the center-of-mass system is
63 10.58 GeV on the $\Upsilon(4S)$ resonance, which enables various physics programs
64 based on the large samples of B mesons, τ leptons, and D mesons. Also, the
65 asymmetric energy of the 7 GeV electron beam and 4 GeV positron beam is
66 adopted for time-dependent CP violation measurements. The target of Su-
67 perKEKB is to accumulate an integrated luminosity of 50 ab^{-1} with peak lu-
68 minosity of about $6 \times 10^{35} \text{ cm}^{-2}\text{s}^{-1}$. In June 2021, SuperKEKB recorded the
69 world's highest instantaneous luminosity of $3.1 \times 10^{34} \text{ cm}^{-2}\text{s}^{-1}$. The data accu-
70 mulated before July 2021 corresponds to an integrated luminosity of 213 fb^{-1} .

71 The Vertex Detector (VXD) is the innermost detector in the Belle II detector

72 system. The VXD has six layers: the inner two layers (layers 1 and 2) are the
 73 Pixel Detector (PXD), and the outer four layers (layers 3 to 6) are the Silicon
 74 Vertex Detector (SVD). The schematic cross-sectional view of the VXD is shown
 75 in Fig. 1. The PXD consists of DEPFET pixel sensors, and its innermost radius
 76 is 1.4 cm from the IP. A detailed description of the SVD appears in Sec. 2.

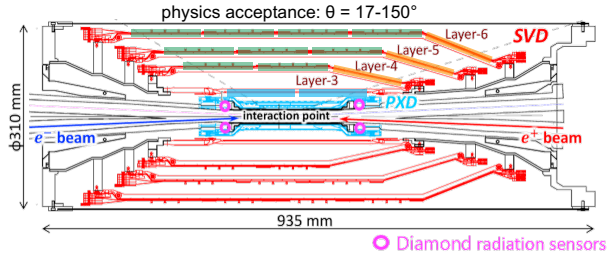


Figure 1: Schematic cross-sectional view of the VXD. The SVD is in red, the PXD in light-blue, and the IP beam pipe diamonds in pink circles. The locations of the three types of DSSDs are indicated by boxes in three colors: blue for small sensors, green for large sensors, and orange for trapezoidal sensors as described in Tab. 1.

77 Besides the VXD, diamond sensors [3] are mounted on the IP beam pipe and
 78 the bellows pipes outside of the VXD. The pink circles in Fig. 1 indicate the
 79 locations of the diamond sensors on the IP beam pipe. They measure the dose
 80 rates in these locations. The measured doses are used to estimate the dose in
 81 the SVD. They also send beam abort requests to SuperKEKB if the radiation
 82 level gets too high to avoid severe damage to the detector.

83 2. Belle II Silicon Vertex Detector

84 The SVD is crucial for extrapolating the tracks to the PXD. This task is
 85 essential for measuring the decay vertices with the PXD and pointing at a
 86 region-of-interest limiting the PXD readout volume. Also, the SVD plays a
 87 critical role in the decay vertex measurement in the case of long-lived particles
 88 like K_S mesons, which decay inside the SVD volume. Other roles of the SVD
 89 are the standalone track reconstruction of low-momentum charged particles and
 90 their particle identification using ionization energy deposits.

91 The SVD [4] consists of four layers of double-sided silicon strip detectors
 92 (DSSDs). The material budget of the SVD is about 0.7% of a radiation length
 93 per layer. The aluminum readout strips are AC-coupled to every other n/p-
 94 side strips (electrodes) on the n-type substrate over the silicon oxide layer. On
 95 each DSSD plane, a local coordinate is defined with u and v : u -axis along n-side
 96 strips and v -axis perpendicular to u -axis. In other words, p-side strips and n-side
 97 strips provide u and v information, respectively. In the cylindrical coordinate, u
 98 corresponds to $r-\varphi$ information and v corresponds to z information. The SVD
 99 consists of three types of sensors: “small” sensors in layer 3, “large” sensors in
 100 the barrel region of layers 4, 5, and 6, and “trapezoidal” sensors in the forward
 101 region of layers 4, 5, and 6, which is slanted. They are indicated in blue, green,
 102 and orange boxes in Fig. 1. The dimensions for these three types of sensors are
 103 summarized in Tab. 1. The sensors are manufactured by two companies: the
 104 small and large sensors by Hamamatsu and trapezoidal sensors by Micron. The
 105 full depletion voltage is 60 V for Hamamatsu sensors, 20 V for Micron sensors;
 106 both types of sensors are operated at 100 V. In total, 172 sensors are assembled,
 107 corresponding to a total sensor area of 1.2 m² and 224,000 readout strips.

	Small	Large	Trapezoidal
No. of u/p-strips	768	768	768
u/p-strip pitch	50 μm	75 μm	50–75 μm
No. of v/n-strips	768	512	512
v/n-strip pitch	160 μm	240 μm	240 μm
Thickness	320 μm	300 μm	300 μm
Manufacturer	Hamamatsu		Micron

Table 1: Table of dimensions for three types of sensors. Only readout strips are taken into account for number of strips and strip pitch.

108 The front-end ASIC used in the SVD is APV25 [5], which was originally
 109 developed for the CMS silicon tracker. The APV25 is radiation hard for a
 110 dose up to 100 Mrad radiation. It has 128 channel inputs and shapers for

111 each channel with a shaping time of about 50 ns. For the SVD, the APV25 is
112 operated in “multi-peak” mode. The mechanism of the data sampling in the
113 multi-peak mode is explained in Fig. 2. The chip samples the height of the
114 signal waveform with the 32 MHz clock and stores each sample’s information
115 in an analog ring buffer. Since the bunch-crossing frequency is eight times
116 faster than the sampling clock, the stored samples are not synchronous to the
117 beam collision, in contrast to CMS, which motivates operation in the multi-
118 peak mode. In the present readout configuration (the six-samples mode), at
119 every reception of the Belle II global Level-1 trigger, the chip reads out six
120 successive samples of the signal waveform stored in the buffers. The six-samples
121 mode offers enough time window ($6/32 \text{ MHz}^{-1} = 187 \text{ ns}$) to accommodate large
122 timing shifts of the trigger. In preparation for operation with higher luminosity,
123 where background occupancy, trigger dead-time, and the data size increase, we
124 developed the three/six-mixed acquisition mode (mixed-mode). The mixed-
125 mode is a new method to read out the signal samples from the APV25, in
126 which the number of the samples changes between three and six in each event,
127 depending on the timing precision of each Level-1 trigger signal in that event.
128 For triggers with good timing precision, three-samples data are read out and the
129 data have half time window and half data size compared to ones of six-samples
130 data, resulting in the reduction of the effect due to higher luminosity. This
131 functionality was already implemented in the running system and confirmed by
132 a few hours of smooth physics data-taking. Before we start to use the mixed-
133 mode, the effect on the performance due to the change of the acquisition mode
134 is to be assessed. As the first step, the effect in the hit efficiency was evaluated
135 as described in Sec. 3.

136 The APV25 chips are mounted on each middle sensor (chip-on-sensor con-
137 cept) with thermal isolation foam in between. The merit of this concept is
138 shorter signal propagation length, leading to smaller capacitance of the signal
139 line and hence reduced noise level. To minimize the material budget the APV25
140 chips on the sensor are thinned down to $100 \mu\text{m}$. APV25s are mounted on a
141 single side of the sensor and readout of the signals is from the other side via

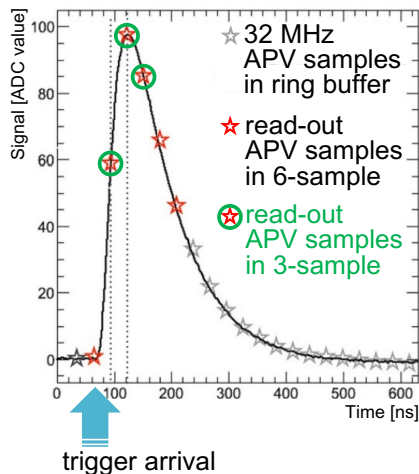


Figure 2: Sampling in the “multi-peak” mode of APV25. The black line shows the signal waveform after the CR-RC shaper circuit. The stars show the sampled signal height recorded in the analog ring buffer according to the 32 MHz sampling clock. The red stars indicate the six successive samples read out at the trigger reception in the six-samples mode. The red stars with a green circle indicate the samples read out in the three-samples acquisition.

142 wrapped flexible printed circuits. The power consumption of the APV25 chip
 143 is 0.4 W/chip and in total 700 W in the entire SVD. The chips are chilled by
 144 bi-phase -20°C CO_2 .

145 3. Performance

146 The SVD was combined with the PXD to complete the VXD assembly in
 147 October 2018, and the VXD was installed to the Belle II detector system in
 148 November 2018. Since March 2019, the SVD has been operating reliably and
 149 smoothly for two and a half years, without any major problems. The total
 150 fraction of masked strips is about 1%. There was only one issue where one
 151 APV25 chip (out of 1,748 chips) was disabled during the spring of 2019, which
 152 was remediated by reconnecting a cable in the summer of 2019.

153 The SVD has also demonstrated stable and excellent performance [6]. The
 154 hit efficiency is continuously over 99% in most of the sensors. The cluster

155 charge distributions are also reasonable. On the u/p-side, the most probable
 156 values agree with the calculated charge amount induced by MIPs within the
 157 uncertainty in calibration. On the v/n-side, 10–30% of the collected charge is
 158 lost compared to MIP due to the smaller inter-strip capacitance of the floating
 159 strips with larger strip pitches than the u/p-side. The most probable values of
 160 the cluster signal-to-noise ratio distributions range from 13 to 30.

161 We measured the cluster position resolution by analyzing the $e^+e^- \rightarrow \mu^+\mu^-$
 162 data [7]. The cluster position resolution is estimated from the residual between
 163 the cluster position and the track position not biased by the target cluster after
 164 subtracting the effect of the track extrapolation error. The cluster position
 165 resolutions for different incident angles are shown in Fig. 3. For normal incident
 166 tracks, it agrees with the expectations from the strip pitch including floating
 167 strips. For tracks with an incident angle, it is expected to get a better resolution,
 168 which is indeed the case in the v/n-side results. However, this effect is not
 169 observed on the u/p-side, and the study is still ongoing to improve the cluster
 170 position estimation.

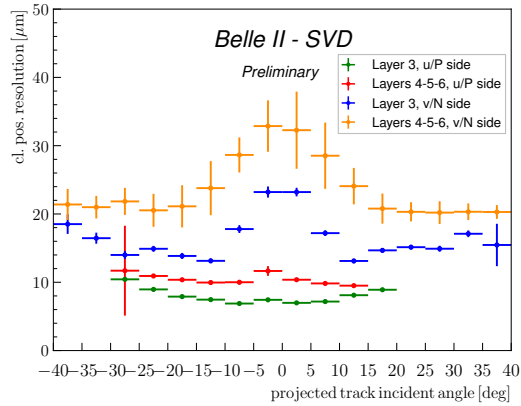


Figure 3: The SVD cluster position resolution depending on the projected track incident angle. The green (blue) plot shows the resolution in the u/p-side (n/v-side) of layer 3 sensors, and the red (yellow) one shows the u/p-side (n/v-side) of layers 4, 5, and 6 sensors.

171 The cluster hit-time resolution was also evaluated in hadron-event¹ data
 172 using the reference event time estimated by the Central Drift Chamber (CDC)
 173 outside of the SVD. The error on the event time, about 0.7 ns, was subtracted
 174 to evaluate the intrinsic SVD hit-time resolution. The resulting resolution is
 175 2.9 ns on the u/p-side and 2.4 ns on the v/n-side. With such precise hit-
 176 time information, it is possible to reject off-time background hits efficiently.
 177 The hit-time distributions for signal² and off-time background³ are shown in
 178 Fig. 4. The signal distribution has a narrow peak, while the background hit-time
 179 distribution is broad and almost flat in the signal peak region. The separation
 180 power of the hit-time is high, as expected. For example, if we reject hits with
 181 the hit-time less than -38 ns in this plot, we can reject 46% of the background
 182 hits while keeping 99% of the signal hits. The background rejection based on
 183 the hit-time is essential to sustain the good tracking performance in the future
 184 high beam background condition.

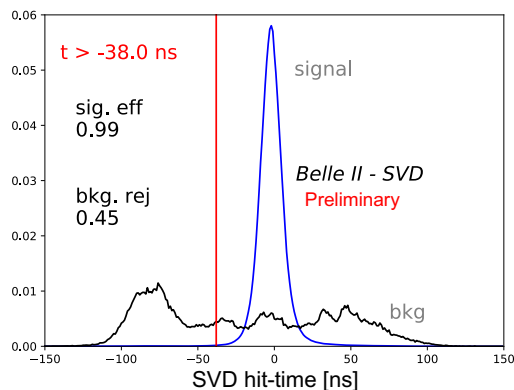


Figure 4: Example of the background hit rejection using hit-time. The blue distribution shows the signal, and the black distribution shows the off-time background. Assuming the hit-time cut at -38 ns, the signal hit efficiency of 99% and the background hit rejection of 46% are achieved.

¹The event with more than three good tracks and not like Bhabha scattering.

²The clusters found to be used in the tracks in the hadron events.

³The clusters in events triggered by delayed-Bhabha pseudo-random trigger.

185 The performance in three-samples data was compared with that in six-
 186 samples data to evaluate the performance in the mixed-mode. If the trigger
 187 timing has no deviation, the three-samples data will show comparable perfor-
 188 mance to the six-samples data because the relevant part of the signal waveform
 189 to evaluate the necessary signal properties, which are the signal height and the
 190 signal timing, can be accommodated in the three-sample's time window. How-
 191 ever, when the trigger has a jitter and the timing shift happens, some part of
 192 the signal waveform can be out of the three-sample's time window, and the
 193 reconstruction performance deteriorates. We examined the effect on the hit ef-
 194 ficiency as a function of the trigger timing shift. The effect is evaluated by the
 195 relative hit efficiency, which is defined as the ratio of the hit efficiency in the
 196 three-samples data to the one in the six-samples data. For this study, the three-
 197 samples data are emulated in the offline analysis from the six-samples data by
 198 selecting consecutive three samples at fixed positions in the six samples. The
 199 trigger timing shift is evaluated by the CDC event time. The resulting relative
 200 efficiencies as a function of the trigger timing shift in the hadron-event data are
 201 shown in Fig. 5. The decreasing trend is observed for the shift of the trigger
 202 timing, as expected. As a result, the relative efficiency is over 99.9% for the
 203 trigger timing shift within ± 30 ns.

204 **4. Beam-related background effects on SVD**

205 The beam-related background increases the hit occupancy of the SVD, which
 206 in turn degrades the tracking performance. Considering this performance degra-
 207 dation, we set the occupancy limit in layer 3 sensors to be about 3%, which will
 208 be loosened roughly by a factor of two after we apply the hit-time rejection
 209 described in Sec. 3. With the current luminosity, the average hit occupancy in
 210 layer 3 sensors is less than 0.5%. However, the projection of the hit occupancy
 211 at the luminosity of $8 \times 10^{35} \text{ cm}^{-2}\text{s}^{-1}$ is about 3% in layer 3 sensors. The
 212 projected occupancy comes from the Monte Carlo (MC) simulation scaled by
 213 the data/MC ratio determined from the beam background data of the current

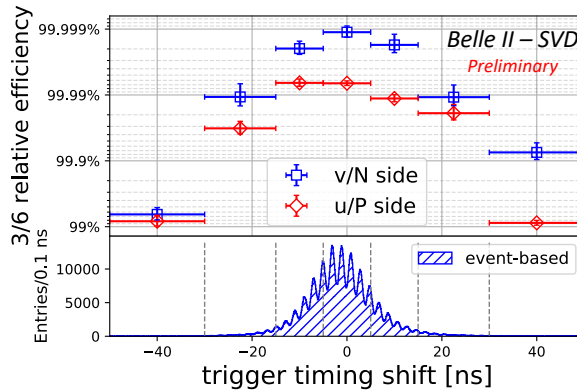


Figure 5: The relative hit efficiencies as a function of the trigger timing shift for v/n-side (blue square) and u/p-side (red diamond). The positive (negative) trigger timing shift corresponds to early (late) trigger timing.

214 beam optics. The corresponding dose is about 0.2 Mrad/smy, and the equivalent
 215 1-MeV neutron fluence is about 5×10^{11} $n_{\text{eq}}/\text{cm}^2/\text{smy}$ (smy: Snowmass Year
 216 $= 10^7$ sec). The long-term extrapolation of the beam background is affected by
 217 large uncertainties from the optimization of collimator settings in MC and the
 218 future evolution of the beam injection background, which is not simulated. This
 219 uncertainty motivates the VXD upgrade which improves the tolerance of the hit
 220 rates and the radiation damage, and the technology assessment is ongoing for
 221 multiple sensor options.

222 From the measured dose on diamond sensors, the integrated radiation dose
 223 in the layer 3 mid-plane sensors, which are the most exposed in the SVD,
 224 is estimated to be 70 krad. The estimation is based on the correlation be-
 225 tween the SVD occupancy and the diamonds dose. The estimated dose in-
 226 cludes uncertainties of about 30% due to the unavailability of the appropri-
 227 ate trigger before December 2020. Assuming the dose/ n_{eq} fluence ratio of
 228 2.3×10^9 $n_{\text{eq}}/\text{cm}^2/\text{krad}$ from MC, 1-MeV equivalent neutron fluence is eval-
 229 uated to be about 1.6×10^{11} $n_{\text{eq}}/\text{cm}^2$ in the first two and a half years.

230 The effect of the integrated dose on the sensor leakage current is measured,
 231 and the results show a clear linear correlation as in the upper plot of Fig. 6.

232 The slopes for all the sensors are summarized in the lower plot of Fig. 6. They
233 are around 2–5 $\mu\text{A}/\text{cm}^2/\text{Mrad}$. The large variations can be explained by tem-
234 perature effects and the deviation of sensor-by-sensor dose from the average in
235 each layer used in the estimation. The slopes are in the same order of magni-
236 tude as previously measured in the BaBar experiment [8], 1 $\mu\text{A}/\text{cm}^2/\text{Mrad}$ at
237 20°C. While the leakage current is increasing, the impact on the strip noise is
238 suppressed by the short shaping time (50 ns) in APV25. It is expected to be
239 comparable to the strip-capacitive noise only after 10 Mrad irradiation and not
240 problematic for ten years where the integrated dose is estimated to be 2 Mrad.

241 The relation between the noise and the integrated dose is shown in Fig. 7.
242 The noise increase of 20–25% is observed in layer 3, but this does not affect the
243 performance of SVD. This noise increase is likely due to the radiation effects on
244 the sensor surface. Fixed oxide charges on sensor surface increase non-linearly,
245 enlarging inter-strip capacitance. The noise saturation is observed on the v/n-
246 side and also starts to be seen on the u/p-side. This behavior agrees with the
247 increase of fixed oxide charges.

248 The full depletion voltage of the sensor is also a key property that can be
249 affected by the radiation damage. It can be measured from the v/n-side strip
250 noise, which suddenly decreases at the full depletion voltage because the sensor
251 substrate is n-type and thus the v/n-side strips can be fully isolated at the full
252 depletion. From this measurement, reasonable full depletion voltages, which are
253 consistent with the values mentioned in Sec. 2, were confirmed, and so far no
254 change in full depletion voltage is observed in the first two and a half years of
255 operation, which is consistent with the expectation from low integrated neutron
256 fluence of $1.6 \times 10^{11} \text{ n}_{\text{eq}}/\text{cm}^2$.

257 5. Conclusions

258 The SVD has been taking data in Belle II since March 2019 smoothly and
259 reliably. The detector performance is excellent and agrees with expectations.
260 We are ready to cope with the increased background during higher luminosity

261 running by rejecting the off-time background hits using hit-time and operating
262 in the three/six-mixed acquisition mode. In the recent study, the efficiency
263 loss in the three-samples data is confirmed to be less than 0.1% for the trigger
264 timing shift within ± 30 ns. The observed first effects of radiation damage are
265 also within expectation and do not affect the detector performance.

266 **Acknowledgments**

267 This project has received funding from the European Union’s Horizon 2020
268 research and innovation programme under the Marie Skłodowska-Curie grant
269 agreements No 644294 and 822070. This work is supported by MEXT, WPI,
270 and JSPS (Japan); ARC (Australia); BMFWF (Austria); MSMT (Czechia);
271 CNRS/IN2P3 (France); AIDA-2020 (Germany); DAE and DST (India); INFN
272 (Italy); NRF-2016K1A3A7A09005605 and RSRI (Korea); and MNiSW (Poland).

273 **References**

- 274 [1] T. Abe, et al., Belle II Technical Design Report (2010). arXiv:1011.0352.
- 275 [2] Y. Ohnishi, et al., Accelerator design at SuperKEKB, Prog. Theor. Exp.
276 Phys. 2013 (3), 03A011 (03 2013).
- 277 [3] S. Bacher, et al., Performance of the diamond-based beam-loss monitor sys-
278 tem of Belle II, Nucl. Instrum. Methods Phys. Res., Sect. A 997 (2021)
279 165157. arXiv:2102.04800.
- 280 [4] K. Adamczyk, et al., The belle ii silicon vertex detector assembly and me-
281 chanics, Nucl. Instrum. Methods Phys. Res., Sect. A 845 (2017) 38–42, pro-
282 ceedings of the Vienna Conference on Instrumentation 2016.
- 283 [5] M. J. French, et al., Design and results from the APV25, a deep sub-micron
284 CMOS front-end chip for the CMS tracker, Nucl. Instrum. Methods Phys.
285 Res., Sect. A 466 (2001) 359–365.

- 286 [6] G. Rizzo, et al., The Belle II Silicon Vertex Detector: Perfor-
287 mance and Operational Experience in the First Year of Data Taking.
288 arXiv:<https://journals.jps.jp/doi/pdf/10.7566/JPSCP.34.010003>.
- 289 [7] R. L. Boucher, et al., Measurement of the cluster position resolution of the
290 Belle II Silicon Vertex Detector, these NIMA Conference Proceedings.
- 291 [8] B. Aubert, et al., The BaBar detector: Upgrades, operation and perfor-
292 mance, Nucl. Instrum. Methods Phys. Res., Sect. A 729 (2013) 615–701.

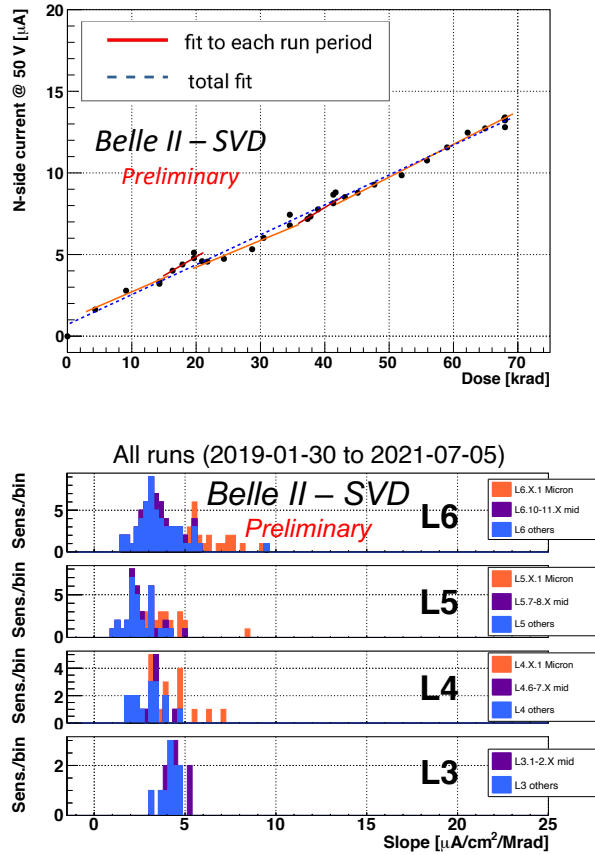


Figure 6: (upper) Effect of the integrated dose on the leakage current in the n/v-side of one sensor in layer 3. The slope is fitted for each run period (solid red line) and for all the runs (dashed blue line). (lower) The fit results of all the sensors for all runs. The sensors are classified as trapezoidal sensors in the forward region (Micron), sensors around the midplane, and the others.

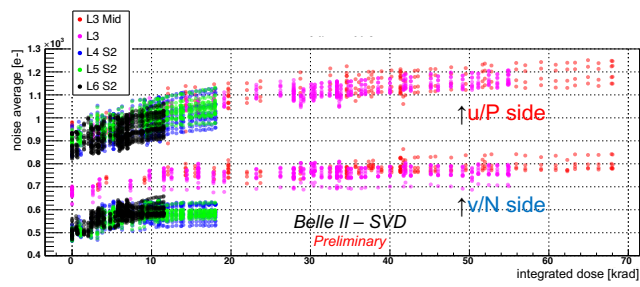


Figure 7: Effect of the integrated dose on the noise average in electron The clear increase is observed and saturated (or start to be saturated) for layer 3 sensors.